

MagicDrive3D: Controllable 3D Generation for Any-View Rendering in Street Scenes

Ruiyuan Gao¹, Kai Chen², Zhihao Li³, Lanqing Hong^{3†}, Zhenguo Li³, Qiang Xu^{1†}

¹CUHK ²HKUST ³Huawei Noah's Ark Lab

{rygao, qxu}@cse.cuhk.edu.hk, kai.chen@connect.ust.hk,
 {zhihao.li, honglanqing, li.zhenguo}@huawei.com

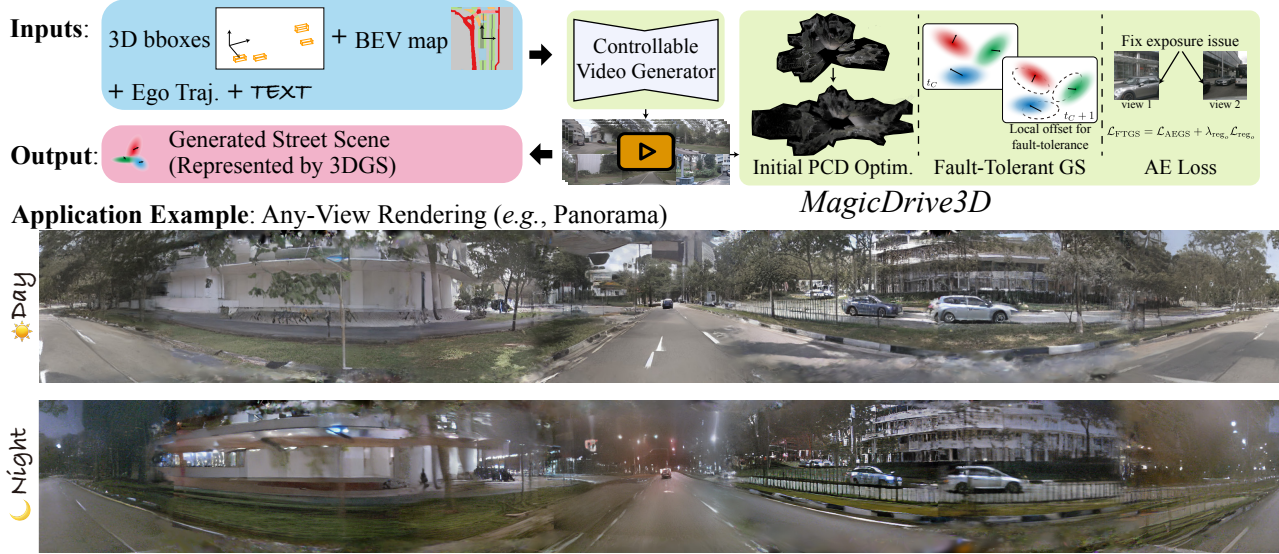


Figure 1. Rendered panorama of the street scene generated from *MagicDrive3D*. With conditional controls from 3D bounding boxes of objects, BEV road map, ego trajectory, and text descriptions (e.g., timeofday), *MagicDrive3D* generates complex open-world 3D scenes represented by deformable Gaussians.

Abstract

Controllable generative models for images and videos have seen significant success, yet 3D scene generation, especially in unbounded scenarios like autonomous driving, remains underdeveloped. Existing methods lack flexible controllability and often rely on dense view data collection in controlled environments, limiting their generalizability across common datasets (e.g., nuScenes). In this paper, we introduce *MagicDrive3D*, a novel framework for controllable 3D street scene generation that combines video-based view synthesis with 3D representation (3DGS) generation. It supports multi-condition control, including road maps, 3D objects, and text descriptions. Unlike previous approaches that require 3D representation before training, *MagicDrive3D* first trains a multi-view video generation model to synthesize diverse street views. This method utilizes routinely collected autonomous driving data, reduc-

ing data acquisition challenges and enriching 3D scene generation. In the 3DGS generation step, we introduce Fault-Tolerant Gaussian Splatting to address minor errors and use monocular depth for better initialization, alongside appearance modeling to manage exposure discrepancies across viewpoints. Experiments show that *MagicDrive3D* generates diverse, high-quality 3D driving scenes, supports any-view rendering, and enhances downstream tasks like BEV segmentation, demonstrating its potential for autonomous driving simulation and beyond.

1. Introduction

The advancement of generative models has enabled their use as data engines, particularly in the realm of controllable generative models, which can produce synthetic data without the need for relabeling [5]. This capability is especially valuable in downstream applications like autonomous driving. However, much of the current research is limited to the generation of 2D data, such as images [5, 33] and

[†]Corresponding authors.

Project Page: <https://flymin.github.io/magicdrive3d/>.

videos [10, 11], which falls short of meeting the demands for data that requires 3D information, such as viewpoint changes [15] or post-generation 3D editing [6]. Consequently, controllable generation of 3D street scenes remains an open challenge.

3D generation¹, on the other hand, can directly produce 3D assets based on given conditions [29, 41], supporting data engine applications that require 3D information. However, many of them focus on single objects [29] or creative scenes [24] for gaming or content creation. Only a few attempts have been made at realistic scene generation for the physical world [2, 14]; for example, NF-LDM [14] enables controllable synthesis of 3D scenes for autonomous driving. The typical workflow for 3D generation involves first obtaining a compact 3D representation (*e.g.*, voxel grids in [14]) and then training a generative model based on this representation. Due to the high demands for data acquisition and reconstruction quality (*e.g.*, the need for static scenes and numerous overlapping camera views), these methods are often limited to specific autonomous driving scenarios (*e.g.*, parking lots, where no objects are moving), and thus do not support common street view datasets (*e.g.*, nuScenes [4]).

These limitations prompt us to reconsider the relationship between the typical 3D generation workflow and 2D controllable generative models in autonomous driving scene generation. We observe that: **1)** 2D controllable generation requires less on data acquisition, as common roadside data can support training; **2)** 2D controllable generation provides the ability to manipulate data (*e.g.*, generating multiple viewpoints of static scenes) to meet the data requirements of 3D reconstruction algorithms; **3)** 3D representation is the core of 3D generation to achieve consistent view rendering and novel view generalization. These observations inspire us to restructure the 3D scene generation workflow by using 2D controllable generation as the initial step, leveraging its data manipulation capabilities to create reconstruction-friendly camera view data, and finally obtain the 3D representation of the scene. This ensures consistent viewpoint rendering and supports applications requiring 3D information (*e.g.*, viewpoint augmentation [15]).

In this paper, we propose *MagicDrive3D*, a novel framework that combines video-based view synthesis and 3D representation (3DGS) generation for controllable 3D street scene generation, as illustrated in Figure 1. Our approach begins with training a multi-view video generation model to synthesize multiple street views. Besides text prompts, this model is configured using conditions from object boxes, road maps, and camera poses to support precise content control for static scene transformation. Additionally, we

¹In this paper, we focus on generative models where views/scenes are generated from latent variables, which is different from reconstruction (*e.g.*, [38]) or view synthesis (*e.g.*, [25]).

incorporate ego trajectory embeddings representing the relative pose transformation between each frame, eliminating the need for pose estimation after view generation, leading to reconstruction-friendly view generation. Next, we identify and solve several drawbacks in existing reconstruction algorithms on generated views. Since artifacts in view generation break the consistency assumption of reconstruction algorithms (*e.g.*, 3DGS [13]), these artifacts can be amplified in the generated 3D representation, resulting in degraded rendering quality. To solve this issue, we improve the 3D representation generation from the perspectives of prior knowledge, modeling, and loss functions. Most importantly, we introduce Fault-Tolerant Gaussian Splatting (FTGS) and appearance embedding maps to handle local inconsistency and exposure discrepancies, respectively.

Demonstrated by extensive experiments, our *MagicDrive3D* framework excels in generating highly realistic street scenes that align with road maps, 3D bounding boxes, and text descriptions, as exemplified in Figure 1. We further show that the generated camera views can augment training of Bird’s Eye View (BEV) segmentation tasks, improving the viewpoint robustness on perception tasks. Notably, *MagicDrive3D* is the first to achieve controllable 3D street scene generation using a common driving dataset (*e.g.*, the nuScenes dataset [4]), without requiring repeated data collection from static scenes or other sensor information.

We summarize our contributions as follows:

- We propose *MagicDrive3D*, the first framework to effectively integrate both view synthesis and 3D representation generation for controllable 3D street scene generation. *MagicDrive3D* generates realistic 3DGS for street scenes that support rendering from any camera view according to various control signals.
- We introduce a relative pose embedding to generate videos with accurate pose controls. Besides, we enhance the 3D representation generation quality through a dedicated pipeline (including Fault-Tolerant Gaussian Splatting) to handle local inconsistency and exposure discrepancies in the generated videos.
- Through extensive experiments, we demonstrate that *MagicDrive3D* generates high-quality street scenes with various controllability. We also show that synthetic data improves 3D perception tasks, highlighting the practical benefits of our approach.

2. Related Work

3D Scene Generation. Numerous 3D-aware generative models can synthesize images with explicit camera pose control [25, 45] and potentially other scene properties [29], but only a few scale for open-ended 3D scene generation. GSN [8] and GAUDI [2], representative of models generating indoor scenes, utilize NeRF [21] with latent code

Table 1. Comparisons on data collection requirements and functionality among different types of methods. *MagicDrive3D* belongs to 3D scene generation but can do more and requires less than previous works. Due to space limits, we only cite some typical works for each category. More detailed related works can be found in Section 2.

Method Type	Data Collection Requirements		Prior Control	Novel Appearance	Novel Pose Rendering	
	Allow Dynamic Scene	Allow Sparse Pose Coverage			Within Trajectory	360°
Reconstruction [6, 18, 22, 30, 35, 40, 44, 48]	✓	✓	✗	✗	✓	✗
Image/Video Generation [10, 11]	✓	✓	✓	✓	✗	✗
3D Scene Generation ([2, 14])	✗	✗	✓	✓	✓	✓
3D Scene Generation (<i>MagicDrive3D</i>)	✓	✓	✓	✓	✓	✓

input for “floorplan” or tri-plane feature. Their reliance on datasets covering different camera poses is incompatible with typical driving datasets where only fixed cameras are available. NF-LDM [14] develops a hierarchical latent diffusion model for scene feature voxel grid generation. However, their representation and complex modeling hinder fine detail generation.

Contrary to previous works focusing on scene generation using explicit geometry, often requiring substantial data not suitable for typical street view datasets (*e.g.*, nuScenes [4]) as discussed in Section 1, we propose merging geometry-free view synthesis with geometry-focused scene representations for controllable street scene creation. Table 1 shows a detailed comparison among different types of methods. Methodologically, inpainting-based methods [7, 16, 42] are most similar to our approach. However, they generally rely on text-controlled image generation models, which cannot qualify as a view synthesis model. Besides, they cannot complete our street scene generation task due to the lack of controllability, as showcased in Appendix G. In contrast, our video generation model is 3D-aware. Besides, we propose several improvements over 3DGS for better scene generation quality.

2D Street View Generation. Diffusion models [12, 28] boost a series of works for 2D street view generation. These works span from single view video (*e.g.*, [31]) to multi-view video (*e.g.*, [11, 32, 36]). Despite cross-view consistency being essential for multi-view video generation, their generalization ability on camera poses is limited due to the data-centric nature [11]. Furthermore, these models lack accurate control over frame transformation (*e.g.*, precise ego trajectory), which is crucial for 3DGS generation. Our work addresses this by enhancing pose control in video generation and proposing a dedicated 3DGS generation pipeline for geometric assurance.

Street Scene Reconstruction. Scene reconstruction (or novel view rendering) for street views is useful in applications like driving simulation, and augmented and virtual reality. For street scenes, attributes like scene dynamic and discrepancies from multi-camera data collection make typical large-scale reconstruction methods ineffective (*e.g.*, Lin et al. [17], Martin-Brualla et al. [19], Rematas et al.

[23]). Hence, real data-based reconstruction methods like Xie et al. [38], Yan et al. [39] utilize LiDAR for depth prior, but their output only permits novel view rendering, lacking the capability of novel scene generation. Unlike these methods, our approach synthesizes novel scenes under multiple levels of conditional controls.

3. Preliminaries

Problem Formulation. In this paper, we focus on controllable street scene generation. Given scene description S_t , our task is to generate street scenes (represented with 3D Gaussians \mathbf{G}) that correspond to the description from a set of latent $\mathbf{z} \sim \mathcal{N}(\mathbf{0}, \mathbf{I})$, *i.e.* $\mathbf{G} = \mathcal{G}(\mathbf{S}_t, \mathbf{z})$. To describe a street scene, we adopt the most commonly used conditions as per Gao et al. [11], Wang et al. [32], Wen et al. [36]. Specifically, a frame of driving scene $\mathbf{S}_t = \{\mathbf{M}_t, \mathbf{B}_t, \mathbf{L}_t\}$ is described by road map $\mathbf{M}_t \in \{0, 1\}^{w \times h \times c}$ (a binary map representing a $w \times h$ meter road area in BEV with c semantic classes), 3D bounding boxes $\mathbf{B}_t = \{(c_i, b_i)\}_{i=1}^N$ (each object is described by box $b_i = \{(x_j, y_j, z_j)\}_{j=1}^8 \in \mathbb{R}^{8 \times 3}$ and class $c_i \in \mathcal{C}$), and text \mathbf{L}_t describing additional information about the scene (*e.g.*, weather and time of day). In this paper, we parameterize all geometric information according to the LiDAR coordinate of the ego car.

One direct application of scene generation is any-view rendering. Specifically, given any camera pose $\mathbf{P} = [\mathbf{K}, \mathbf{R}, \mathbf{t}]$ (*i.e.*, intrinsics, rotation, and translation), the 3DGS model $\mathbf{G}(\cdot)$ should render photo-realistic views of the generated scene with 3D consistency, $\mathcal{I}^r = \mathbf{G}(\mathbf{P})$, which is not applicable to previous street view generation (*e.g.*, Gao et al. [11], Wang et al. [32], Wen et al. [36]). Besides, we present more practical applications in Section 5.

3D Gaussian Splatting. We briefly introduce 3DGS since our scene representation is based on it. 3DGS [13] represents the geometry and appearance via a set of 3D Gaussians \mathbf{G} . Each 3D Gaussian is characterized by its position $\boldsymbol{\mu}_p$, anisotropic covariance $\boldsymbol{\Sigma}_p$, opacity α_p , and spherical harmonic coefficients for view-dependent colors c_p . Given a sparse point cloud \mathcal{P} and several camera views $\{\mathcal{I}_i\}$ with poses $\{\mathbf{P}_i\}$, a point-based volume rendering [49] is applied to make Gaussians optimizable through gradient descend and interleaved point densification. Specifically, the loss is

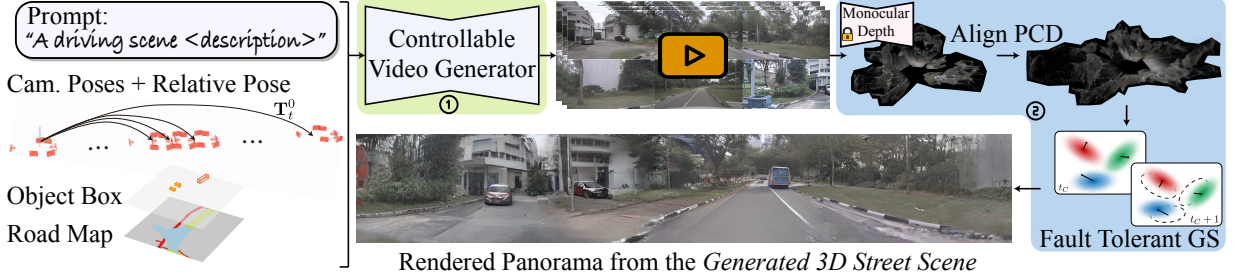


Figure 2. Method Overview of *MagicDrive3D*. For controllable street scene generation, *MagicDrive3D* decomposes the task into two steps: ① conditional multi-view video generation, which tackles the control signals and generates consistent view priors to the novel scene; and ② Gaussian Splatting generation with our Enhanced GS pipeline, which supports various viewpoint rendering (e.g., panorama).

as Equation 1, where \mathcal{I}^r is the rendered image, λ is a hyper-parameter, and $\mathcal{L}_{\text{D-SSIM}}$ denotes the D-SSIM loss [13].

$$\mathcal{L}_{\text{GS}} = (1 - \lambda)\mathcal{L}_1(\mathcal{I}_i^r, \mathcal{I}_i) + \lambda\mathcal{L}_{\text{D-SSIM}}(\mathcal{I}_i^r, \mathcal{I}_i) \quad (1)$$

4. Methods

In this section, we introduce our controllable street scene generation pipeline. Due to the challenges that exist in data collection, we integrate geometry-free view synthesis and geometry-focused 3DGS generation, detailed in Section 4.1 and Figure 2. Specifically, we introduce a controllable video generation model to connect control signals and 3DGS generation by camera views generation (Section 4.2). Besides, we present a dedicated 3DGS generation pipeline for generated views, enhancing from prior, modeling, and loss perspectives (Section 4.3).

4.1. Overview of *MagicDrive3D*

Direct modeling of controllable street scene generation faces two major challenges: scene dynamics and discrepancy in data collection. *Scene dynamics* refers to the movements and deformation of elements in the scene, while *discrepancy in data collection* refers to the discrepancy (e.g., exposure) caused by data collection. These two challenges are even more severe due to the sparsity of cameras for street views (e.g., typically only 6 surrounding perspective cameras). Therefore, reconstruction-generation frameworks do not work well for street scene generation [2, 14].

Figure 2 shows the overview of *MagicDrive3D*. Given scene descriptions \mathbf{S} as input, *MagicDrive3D* first extend the descriptions into sequence $\{\mathbf{S}_t\}$, where $t \in [0, T]$ according to preset camera poses $\{\mathbf{P}_{c,t}\}$, and generate a sequence of successive multi-view images $\{\mathcal{I}_{c,t}\}$, where $c \in \{1, \dots, N\}$ refers to N surrounding cameras, according to conditions $\{\mathbf{S}_t, \mathbf{P}_{c,t}\}$ (detailed in Section 4.2). Then we generate 3D Gaussian representation of the scene with $\{\mathcal{I}_{c,t}\}$ and camera poses $\{\mathbf{P}_{c,t}\}$ as input. This step contains an initializing procedure with a pre-trained monocular depth model and an optimizing process with Fault-Tolerant Gaussian Splatting (FTGS, detailed in Section 4.3). Consequently, the generated street scene reflects different control

signals accurately and supports any-view rendering.

MagicDrive3D integrates geometry-free view synthesis and GS-based scene representation, which are geometry-focused. Specifically, control signals are tackled by a multi-view video generator, while the 3DGS generation step guarantees the generalization ability for any-view rendering. Such a video generator has two advantages: first, since multi-view video generation does not require generalization on novel views [11], it poses less data dependency for street scenes; second, through conditional training, the model is able to decompose control signals, turning dynamic scenes into static scenes that are more friendly for 3DGS generation. Besides, for the 3DGS generation step, strong priors from the multi-view video reduce the burden for scene modeling with complex details.

4.2. Video Generation with Relative Pose Control

Given scene descriptions and a sequence of camera poses $\{\mathbf{S}_t, \mathbf{P}_{c,t}\}$, our video generator is responsible for multi-view video generation. Although many previous arts for street view generation achieve expressive visual effects (e.g., [11, 31, 32, 36]), their formulations leave out a crucial requirement for 3D modeling. Specifically, the camera pose $\mathbf{P}_{c,t}$ they use is typically relative to the LiDAR coordinate of each frame. Thus, there is no precise control signal related to the ego trajectory, which significantly determines the geometric relationship between views of different t s.

In our video generation model, we amend such precise control ability by adding the transformation between each frame to the first frame, *i.e.*, \mathbf{T}_t^0 . To properly encode such information, we adopt Fourier embedding with Multi-Layer Perception (MLP), and concatenate the embedding with the original embedding of $\mathbf{P}_{c,t}$, similar to Gao et al. [11]. As a result, our video generator provides better temporal quality across frames, most importantly, making the camera poses to each view available in the same coordinate, *i.e.*, $[\mathbf{R}_{c,t}^0, \mathbf{t}_{c,t}^0] = \mathbf{T}_t^0[\mathbf{R}_{c,t}, \mathbf{t}_{c,t}]$.

4.3. Enhanced FTGS for 3DGS Generation

As introduced in Section 3, 3DGS is a flexible explicit representation for 3D scenes. Besides, the fast training and ren-

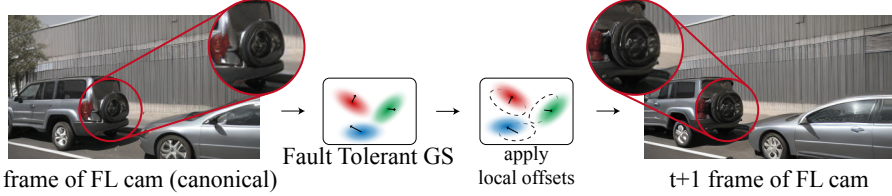


Figure 3. Illustration of the local inconsistency from two successive generated frames of Front-Left (FL) camera. Even though our video generation model retains fine 3D consistency, minor discrepancies are inevitable. Our FTGS can effectively reconstruct the scene with awareness of such discrepancy.

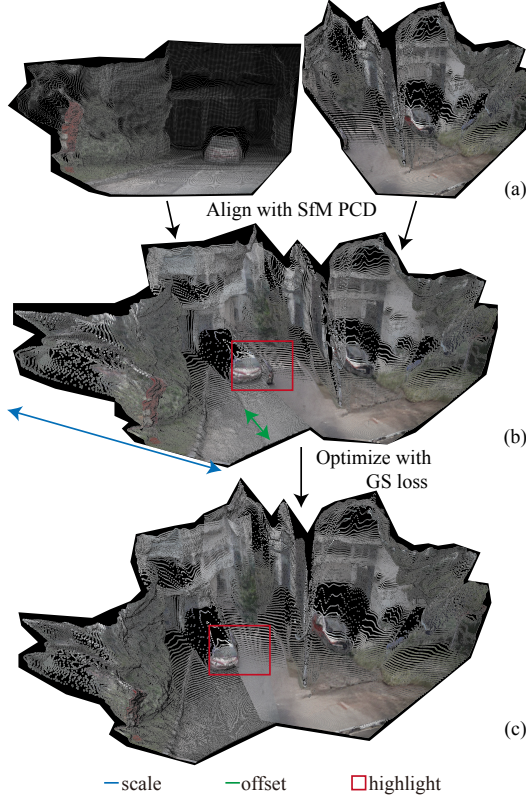


Figure 4. We optimize the monocular depths (a) with 2 steps for better alignment: coarse scale/offset estimation with SfM PCD (b) and GS optimization (c).

dering speed of 3DGS makes it highly suitable for reducing generation costs in our scene creation pipeline. However, similar to other 3D reconstruction methods, 3DGS necessitates high cross-view 3D consistency at the pixel level, which unavoidably magnifies the minor artifacts in the generated data into conspicuous errors. Therefore, we propose improvements for 3DGS from the perspectives of *prior*, *modeling*, and *loss*, enabling 3DGS to tolerate minor artifacts in the generated camera view from our video generation model, thereby becoming a potent tool for enhancing geometric consistency in rendering.

Prior: Consistent Depth Prior. As essential geometry information, depth is extensively utilized in street scene reconstruction, such as the depth value from LiDAR or other depth sensors used by Yan et al. [39]. However, for synthesized camera views, LiDAR/depth information is unavail-

able (also making these methods not suitable for our scenario). Therefore, we propose to use a pre-trained monocular depth estimator [3] to infer depth information.

While monocular depth estimation is separate for each camera view, proper scale $s_{c,t}$ and offset $b_{c,t}$ parameters should be estimated to align them for a single scene [47], as in Figure 4(a). To this end, we first apply the Point Cloud (PCD) from Structure of Motion (SfM) [26, 27] for estimation, shown in Figure 4(b). However, such PCD is too sparse to accurately restore $(s_{c,t}, b_{c,t})$ for any views. To bridge the gap, secondly, we propose further optimizing the $(s_{c,t}, b_{c,t})$ using the GS loss, as in Figure 4(c). Specifically, we replace the optimization for Gaussian centers μ_i with $(s_{c,t}, b_{c,t})$. After the optimization, we reset μ_i with points from depth values. Since GS algorithm is sensitive to accurate point initialization [9, 13], our method provides a useful prior for 3DGS generation in this sparse view scenario.

Modeling: Fault-Tolerant Gaussians for Local Inconsistency. Despite the 3D geometric consistency provided by our video generation model, there are inevitably pixel-level disparities in some object details, as shown in Figure 3. Even worse, the strict consistency assumption of 3DGS [13] (and all other reconstruction algorithms, *e.g.*, [37, 38, 48]) can amplify these minor errors, resulting in floater artifacts. To mitigate the impact of these errors, we propose Fault-Tolerant Gaussian Splitting (FTGS), which reduces the requirement for temporal consistency between frames, thereby ensuring the 3DGS generation quality in the canonical space from the generated views.

Specifically, as shown in Figure 3, we pick the center frame $t = t_C$ as the canonical space and enforce all Gaussians in this space. Then, we allocate a set of offsets to each Gaussian, $\mu_p^o(t) \in \mathbb{R}^3$, where $t \in [1, \dots, T]$ and $\mu_p^o(t_C) \equiv \mathbf{0}$. Note that, different camera views from the same t share the same $\mu_p^o(t)$ for each Gaussian, and we apply regularization on them to keep the offsets in local, as shown in Equation 2:

$$\mathcal{L}_{\text{reg}_o} = \|\mu_p^o(t)\|_2. \quad (2)$$

Consequently, $\mu_p^o(t)$ can manage the local inconsistency driven by pixel-level disparities, while μ focuses on the global geometric correlations. It ensures the quality of scene 3DGS generation by leveraging consistent parts across different viewpoints, simultaneously eliminating ar-

NeuralField-LDM (w/ in-house dataset)



Ours (w/ nuScenes dataset)

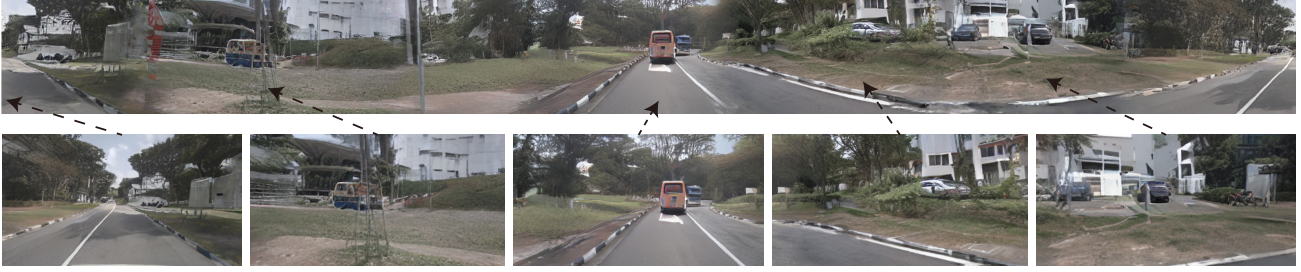


Figure 5. Qualitative comparison with NF-LDM [14]. Our method can generate higher quality 3D scenes while maintaining better object geometry, with stronger controllability compared to NF-LDM (see the significant object deformation in NF-LDM). Panoramas for GS are transformed and stitched from perspective cameras with 90° FOV. Views in the last row are rendered with unseen camera rigs of nuScenes.

tifacts. Besides, with the analytical gradient w.r.t. $SE(3)$ pose of cameras [20], we make the camera pose optimizable in the final few steps of GS iterations, which helps to mitigate the local inconsistency from camera poses.

Loss: Aligning Exposure with Appearance Modeling. Typical street view datasets are collected using multiple cameras, each operating independently with auto-exposure and auto-white-balance [4]. Appearance modeling addresses issues from such in-the-wild reconstructions [19]. Similarly, video generation is optimized to match the real data distribution, so differences between cameras also appear in generations. We propose a dedicated appearance modeling technique for GS representation as a solution.

We hypothesize that the disparity between different views can be represented by affine transformations $\mathbf{A}_i(\cdot)$ for i -th camera view. An Appearance Embedding (AE) map $\mathbf{e}_i \in \mathbb{R}^{w_e \times h_e \times c_e}$ is allocated for each view, and a Convolutional Neural Network (CNN) is utilized to approximate this transformation matrix $w_{\mathbf{A}} \in \mathbb{R}^{w \times h \times 3}$ (Appendix H contains more details). The final computation of the pixel-wise ℓ_1 loss is conducted using the transformed image.

Therefore, our final loss for FTGS is as Equation 3, where λ_{reg_o} is the hyper-parameter for offset regularization.

$$\begin{aligned} \mathcal{L}_{\text{FTGS}} &= \mathcal{L}_{\text{AEGS}} + \lambda_{\text{reg}_o} \mathcal{L}_{\text{reg}_o} \\ &= (1 - \lambda) \mathcal{L}_1(\mathbf{A}_i(\mathcal{I}_i^r), \mathcal{I}_i) + \lambda \mathcal{L}_{\text{D-SSIM}}(\mathcal{I}_i^r, \mathcal{I}_i) + \lambda_{\text{reg}_o} \mathcal{L}_{\text{reg}_o} \end{aligned} \quad (3)$$

Appendix C holds a full description of the algorithm.

5. Experiments

5.1. Experimental Setup

Dataset. We test *MagicDrive3D* using nuScenes dataset [4], which is commonly used for generating and reconstructing street views [11, 32, 36, 38]. The official configuration is followed (700 street-view video clips of ~ 20 s each for training and another 150 clips for validation). For

Methods	FVD	FID (seen)	FID (novel)
MagicDrive	177.26	20.92	N/A
<i>MagicDrive3D</i> (video gen.)	164.72	20.67	N/A
3DGS	N/A	45.07	145.72
<i>MagicDrive3D</i> (scene gen.)	N/A	23.99	34.45

Table 2. Generation quality evaluation. We adopt all val. scenes from nuScenes. All generated views are used for 3DGS generation. Novel views using camera poses different from nuScenes.

semantics in control signals, we follow Gao et al. [11], using 10 object classes and 8 road classes.

Metrics and Settings. There is no direct metric for 3D scene generation. Following Kim et al. [14], we primarily evaluate *MagicDrive3D* using the Fréchet Inception Distance (FID) by rendering novel views unseen in the dataset and comparing their FID with real images.

To further demonstrate the effectiveness of each component within our framework, we conducted ablated studies on the improvements in video generation capabilities and the enhancements in content reconstruction quality. The method’s video generation ability is evaluated using Fréchet Video Distance (FVD). Appendix B holds more details.

5.2. Main Results

Generation Quality. In Table 2, generation quality is evaluated in two ways. First, 3D scene quality is assessed by FID of rendered views (last row of Table 2), with qualitative comparisons in Figure 5. Lacking a quantitative baseline, we compare our pipeline’s renderings with 3DGS. The last two rows of Table 2 show that our enhanced FTGS improves visual quality, especially in novel views. Second, video quality is assessed using extended 16-frame *MagicDrive* [11] as a baseline. *MagicDrive3D* significantly boosts video quality (shown by FVD), proving the effectiveness of the proposed relative camera pose embedding for enhancing temporal quality. More qualitative comparisons can be

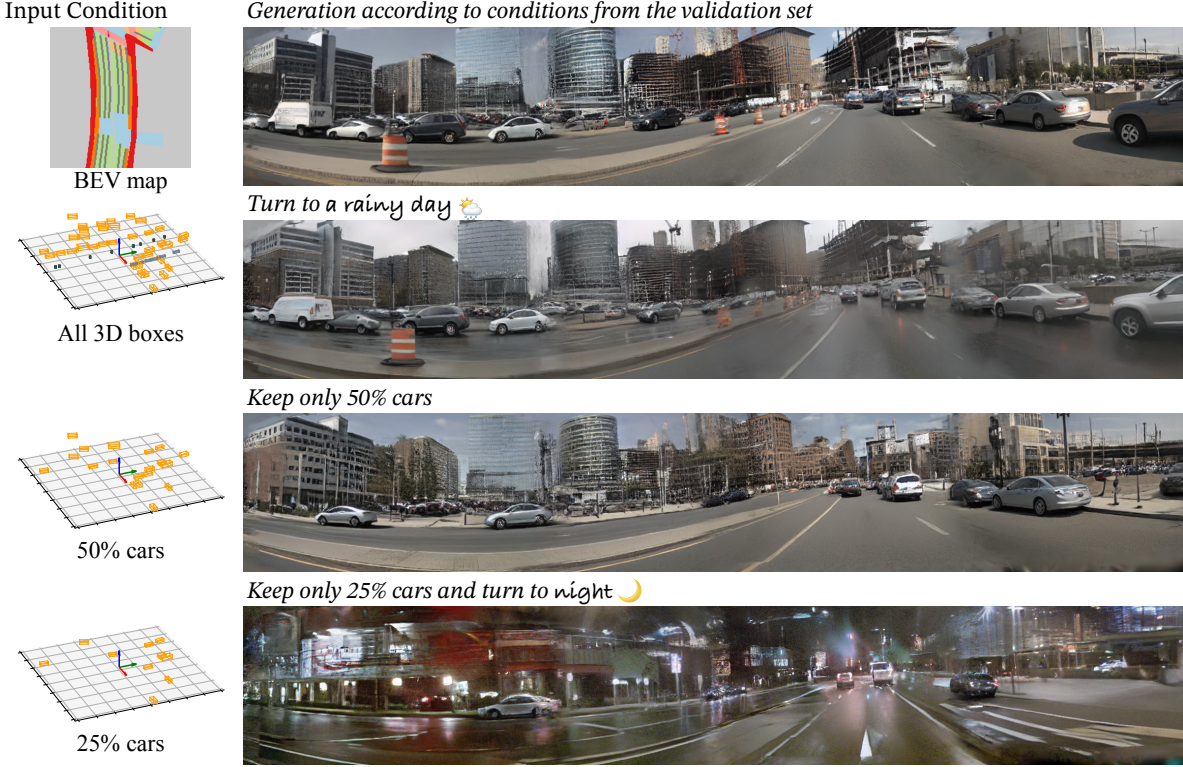


Figure 6. Qualitative evaluation for controllability (we show the view from back-left to front-right area). By changing different control signals, *MagicDrive3D* can edit the scene from different levels.

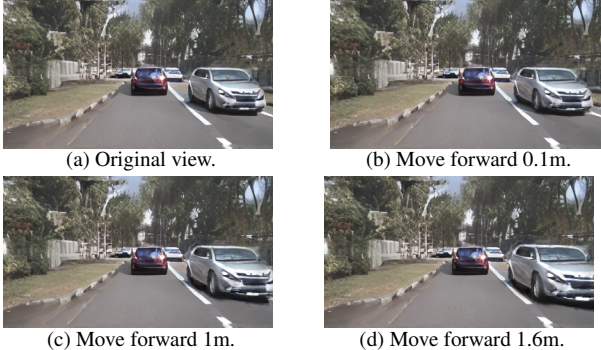


Figure 7. Application of rendering object-level dynamics. After scene generation, we can segment and move the vehicle (the one on the right) in 3D to render a dynamic object.

found in Appendix G.

Controllability. *MagicDrive3D* accepts 3D bounding boxes, BEV map, and text as control signals, each of which possesses the capacity to independently manipulate the scene. Figure 6 shows such controllability, where we edit a scene from the nuScenes validation set. Clearly, *MagicDrive3D* effectively alters the scene generation to align with various control signals.

Furthermore, Section 5.3 shows that the rendered views of the generated scenes can be used as training data to improve the performance of perception models. Such results can serve as further evidence of the controllability.

5.3. Data Augmentation for Perception Tasks

We demonstrate that street 3D scene generation can serve as a data engine for perception tasks, leveraging the advantage of any-view rendering ability of our method to improve viewpoint robustness for perception models [15]. We employ CVT [46] and the BEV segmentation task following the evaluation protocols of Gao et al. [11], Zhou and Krähenbühl [46]. By incorporating 4 different rigs on the FRONT camera and adding rendered views for training, the negative impact from viewpoint changes is alleviated (Table 3), exemplifying the utility of street scene generation in training perception tasks.

5.4. Application: Render Object-level Dynamic

MagicDrive3D is capable of generating 3DGS representations of scenes, which facilitates various applications in scene editing. Our method utilizes metric scale modeling, guaranteeing that any modifications made to the scenes accurately reflect real-world physical distances. As illustrated in Figure 7, we segmented the generated GS and repositioned the object on the right. The resulting scene GS supports rendering effectively.

5.5. Ablation Study

Effectiveness of the Enhanced GS pipeline. We first show the effectiveness of the proposed enhanced GS pipeline

Setting	Method	no rig	depth+0.5m	pitch-5°	yaw+5°	yaw-5°
vehicle	only real data	17.14	16.63	15.50	16.99	15.94
	w/ render view (no rig)	20.67 +3.53	20.13 +3.50	17.03 +1.53	19.40 +2.41	19.30 +3.36
	w/ random aug. of 4 rigs	21.05 +3.91	20.46 +3.83	19.75 +4.25	19.81 +2.82	19.83 +3.89
road	only real data	54.94	54.56	53.82	54.20	53.67
	w/ render view (no rig)	60.31 +5.37	59.93 +5.37	58.46 +4.64	59.16 +4.96	59.32 +5.65
	w/ random aug. of 4 rigs	60.59 +5.65	60.38 +5.82	59.95 +6.13	60.21 +6.01	60.29 +6.62

Table 3. *MagicDrive3D* improves the viewpoint robustness [15] of CVT [46]. All results are mIoU for BEV segmentation. Colors highlight the differences with baseline. The best results are in **bold**.

Settings	Methods	L1 ↓	PSNR ↑	SSIM ↑	LPIPS ↓
train view	3DGS	0.0189	30.1191	0.9261	0.1259
	3DGS + cc	0.0186	30.2498	0.9253	0.1258
	Ours	0.0167	32.6001	0.9544	0.0673
test view	3DGS	0.0202	29.4943	0.9187	0.1365
	3DGS + cc	0.0199	29.6327	0.9178	0.1366
	Ours	0.0174	32.2104	0.9530	0.0693
360°	3DGS	0.0890	17.9879	0.4378	0.4648
	3DGS + cc	0.0799	19.1387	0.4814	0.4697
	Ours	0.0738	19.7063	0.5145	0.4115

Table 4. Performance comparison between the enhanced GS and its baseline. We randomly sample 100 scenes from the nuScenes val. set for evaluation. “cc” refers to color correction from [1]. Although 3DGS does not consider appearance differences, we apply “cc” to it for fair comparisons.

Methods	L1 ↓	PSNR ↑	SSIM ↑	LPIPS ↓
vary-t setting:				
3DGS	0.0799	19.1387	0.4814	0.4697
w/o AE	0.0822	18.8467	0.4758	0.4452
w/o depth scale opt.	0.0815	18.8885	0.4767	0.4366
w/o depth opt.	0.1046	17.2776	0.4399	0.5545
w/o xyz offset + cam	0.0798	19.1657	0.4919	0.4580
Ours	0.0738	19.7063	0.5145	0.4115
360° setting:				
3DGS	0.0804	19.0773	0.4777	0.4796
w/o AE	0.0722	19.7742	0.5114	0.3791
w/o depth scale opt.	0.0736	19.6501	0.5086	0.3736
w/o depth opt.	0.0995	17.6707	0.4487	0.5150
w/o xyz offset + cam	0.0798	19.1682	0.4888	0.4663
Ours	0.0622	21.0351	0.5754	0.3207

Table 5. Ablation study on each component of the enhanced GS, with settings in Table I (appendix) and 100 random scenes from the nuScenes validation set.

through an experimental setting similar to the evaluation of a general reconstruction method [13], *i.e.*, comparing renderings with ground truth (GT) images, with 3DGS [13] as the baseline method. Specifically, two testing scenarios are

employed (as shown in Table I, appendix) : 360°, where all six views from $t = 9$ are reserved for testing; and vary-t, where one view is randomly sampled from different t to assess long-range reconstruction ability through t . Here, the views generated by the video generator are treated as GT. Performance is assessed using L1, PSNR, SSIM [34], and LPIPS [43], as per Kerbl et al. [13].

Among all the metrics in Table 4, our enhanced GS not only improves reconstruction quality for training views but also drastically enhances generalization quality for testing views, compared to 3DGS. We also include more comparison with 4DGS [37] as another baseline in Appendix E.

Ablation on Enhanced Gaussian Splatting. As detailed in Section 4.3, three enhancements—prior, modeling, and loss—were made to 3DGS. To evaluate their efficacy, each was ablated from the final algorithm, with results shown in Table 5. Notations “w/o depth scale opt.” and “w/o depth opt.” indicate the absence of GS loss optimization for $(s_{c,t}, b_{c,t})$ and the use of direct output from the monocular depth model, respectively. Removing each component reduced performance, and incorrect depth sometimes performed worse than the 3DGS baseline. Removing AE in “vary-t” led to lower PSNR but improved LPIPS, as AE mitigates pixel-wise color constraints during 3DGS generation.

Appendix D contains more ablation studies.

6. Conclusion and Discussion

This paper introduces *MagicDrive3D*, a novel framework for controllable 3D street scene generation that integrates multi-view video synthesis with 3D representations. *MagicDrive3D* uses a relative pose embedding in video generation to enhance inter-frame quality while providing camera pose data for each view. The enhanced fault-tolerant GS in *MagicDrive3D* improves 3DGS generation quality from the generated camera views. Consequently, *MagicDrive3D* significantly reduces data collection requirements, enabling training on standard autonomous driving datasets such as nuScenes. Comprehensive experiments demonstrate that *MagicDrive3D* can produce high-quality 3D street scenes with multi-level controls. Furthermore, the generated scenes enhance viewpoint robustness in perception tasks like BEV segmentation.

References

[1] Jonathan T. Barron, Ben Mildenhall, Dor Verbin, Pratul P. Srinivasan, and Peter Hedman. Mip-nerf 360: Unbounded anti-aliased neural radiance fields. In *CVPR*, 2022. 8

[2] Miguel Angel Bautista, Pengsheng Guo, Samira Abnar, Walter Talbott, Alexander Toshev, Zhuoyuan Chen, Laurent Dinh, Shuangfei Zhai, Hanlin Goh, Daniel Ulbricht, et al. Gaudi: A neural architect for immersive 3d scene generation. In *NeurIPS*, 2022. 2, 3, 4

[3] Shariq Farooq Bhat, Reiner Birk, Diana Wofk, Peter Wonka, and Matthias Müller. Zoedepth: Zero-shot transfer by combining relative and metric depth. *arXiv preprint arXiv:2302.12288*, 2023. 5, 1

[4] Holger Caesar, Varun Bankiti, Alex H Lang, Sourabh Vora, Venice Erin Liang, Qiang Xu, Anush Krishnan, Yu Pan, Giancarlo Baldan, and Oscar Beijbom. nuscenes: A multi-modal dataset for autonomous driving. In *CVPR*, 2020. 2, 3, 6

[5] Kai Chen, Enze Xie, Zhe Chen, Yibo Wang, Lanqing HONG, Zhenguo Li, and Dit-Yan Yeung. Geodiffusion: Text-prompted geometric control for object detection data generation. In *ICLR*, 2024. 1

[6] Ziyu Chen, Jiawei Yang, Jiahui Huang, Riccardo de Lutio, Janick Martinez Esturo, Boris Ivanovic, Or Litany, Zan Gojcic, Sanja Fidler, Marco Pavone, Li Song, and Yue Wang. Omnidre: Omni urban scene reconstruction. In *ICLR*, 2025. 2, 3

[7] Jaeyoung Chung, Suyoung Lee, Hyeongjin Nam, Jaerin Lee, and Kyoung Mu Lee. Luciddreamer: Domain-free generation of 3d gaussian splatting scenes. *arXiv preprint arXiv:2311.13384*, 2023. 3, 4

[8] Terrance DeVries, Miguel Angel Bautista, Nitish Srivastava, Graham W Taylor, and Joshua M Susskind. Unconstrained scene generation with locally conditioned radiance fields. In *ICCV*, 2021. 2

[9] Zhiwen Fan, Wenyan Cong, Kairun Wen, Kevin Wang, Jian Zhang, Xinghao Ding, Danfei Xu, Boris Ivanovic, Marco Pavone, Georgios Pavlakos, Zhangyang Wang, and Yue Wang. Instantspat: Unbounded sparse-view pose-free gaussian splatting in 40 seconds. *arXiv preprint arXiv:2403.20309*, 2024. 5

[10] Ruiyuan Gao, Kai Chen, Bo Xiao, Lanqing Hong, Zhenguo Li, and Qiang Xu. Magicdrive-v2: High-resolution long video generation for autonomous driving with adaptive control. *arXiv preprint arXiv:2411.13807*, 2024. 2, 3

[11] Ruiyuan Gao, Kai Chen, Enze Xie, Lanqing Hong, Zhenguo Li, Dit-Yan Yeung, and Qiang Xu. MagicDrive: Street view generation with diverse 3d geometry control. In *ICLR*, 2024. 2, 3, 4, 6, 7, 1

[12] Jonathan Ho, Ajay Jain, and Pieter Abbeel. Denoising diffusion probabilistic models. In *NeurIPS*, 2020. 3

[13] Bernhard Kerbl, Georgios Kopanas, Thomas Leimkühler, and George Drettakis. 3d gaussian splatting for real-time radiance field rendering. *ACM Transactions on Graphics*, 42(4), 2023. 2, 3, 4, 5, 8

[14] Seung Wook Kim, Bradley Brown, Kangxue Yin, Karsten Kreis, Katja Schwarz, Daiqing Li, Robin Rombach, Antonio Torralba, and Sanja Fidler. Neuralfield-ldm: Scene generation with hierarchical latent diffusion models. In *CVPR*, 2023. 2, 3, 4, 6

[15] Tzofi Klinghoffer, Jonah Phlion, Wenzheng Chen, Or Litany, Zan Gojcic, Jungseock Joo, Ramesh Raskar, Sanja Fidler, and Jose M Alvarez. Towards viewpoint robustness in bird’s eye view segmentation. In *ICCV*, 2023. 2, 7, 8

[16] Hanwen Liang, Junli Cao, Vudit Goel, Guocheng Qian, Sergei Korolev, Demetri Terzopoulos, Konstantinos N Plataniotis, Sergey Tulyakov, and Jian Ren. Wonderland: Navigating 3d scenes from a single image. *arXiv preprint arXiv:2412.12091*, 2024. 3

[17] Jiaqi Lin, Zhihao Li, Xiao Tang, Jianzhuang Liu, Shiyong Liu, Jiayue Liu, Yangdi Lu, Xiaofei Wu, Songcen Xu, Youliang Yan, and Wenming Yang. Vastgaussian: Vast 3d gaussians for large scene reconstruction. In *CVPR*, 2024. 3

[18] Kunhao Liu, Ling Shao, and Shijian Lu. Novel view extrapolation with video diffusion priors. *arXiv preprint arXiv:2411.14208*, 2024. 3

[19] Ricardo Martin-Brualla, Noha Radwan, Mehdi S. M. Sajjadi, Jonathan T. Barron, Alexey Dosovitskiy, and Daniel Duckworth. NeRF in the Wild: Neural Radiance Fields for Unconstrained Photo Collections. In *CVPR*, 2021. 3, 6

[20] Hidenobu Matsuki, Riku Murai, Paul H. J. Kelly, and Andrew J. Davison. Gaussian Splatting SLAM. In *CVPR*, 2024. 6

[21] Ben Mildenhall, Pratul P Srinivasan, Matthew Tancik, Jonathan T Barron, Ravi Ramamoorthi, and Ren Ng. Nerf: Representing scenes as neural radiance fields for view synthesis. In *ECCV*, 2020. 2

[22] Chaojun Ni, Guosheng Zhao, Xiaofeng Wang, Zheng Zhu, Wenkang Qin, Guan Huang, Chen Liu, Yuyin Chen, Yida Wang, Xueyang Zhang, et al. Recondreamer: Crafting world models for driving scene reconstruction via online restoration. *arXiv preprint arXiv:2411.19548*, 2024. 3, 1

[23] Konstantinos Rematas, Andrew Liu, Pratul P. Srinivasan, Jonathan T. Barron, Andrea Tagliasacchi, Tom Funkhouser, and Vittorio Ferrari. Urban radiance fields. In *CVPR*, 2022. 3

[24] Foundation AI Team Roblox. Cube: A roblox view of 3d intelligence. *arXiv preprint arXiv:2503.15475*, 2025. 2

[25] Robin Rombach, Patrick Esser, and Björn Ommer. Geometry-free view synthesis: Transformers and no 3d priors. In *ICCV*, 2021. 2

[26] Johannes Lutz Schönberger and Jan-Michael Frahm. Structure-from-motion revisited. In *CVPR*, 2016. 5

[27] Johannes Lutz Schönberger, Enliang Zheng, Marc Pollefeys, and Jan-Michael Frahm. Pixelwise view selection for unstructured multi-view stereo. In *ECCV*, 2016. 5

[28] Yang Song, Jascha Sohl-Dickstein, Diederik P Kingma, Abhishek Kumar, Stefano Ermon, and Ben Poole. Score-based generative modeling through stochastic differential equations. In *ICLR*, 2020. 3

[29] Jiaxiang Tang, Jiawei Ren, Hang Zhou, Ziwei Liu, and Gang Zeng. Dreamgaussian: Generative gaussian splatting for efficient 3d content creation. In *ICLR*, 2024. 2

[30] Qitai Wang, Lue Fan, Yuqi Wang, Yuntao Chen, and Zhaoxiang Zhang. Freevs: Generative view synthesis on free driving trajectory. *arXiv preprint arXiv:2410.18079*, 2024. 3

[31] Xiaofeng Wang, Zheng Zhu, Guan Huang, Xinze Chen, Jia-gang Zhu, and Jiwen Lu. Drivedreamer: Towards real-world-driven world models for autonomous driving. *arXiv preprint arXiv:2309.09777*, 2023. 3, 4

[32] Yuqi Wang, Jiawei He, Lue Fan, Hongxin Li, Yuntao Chen, and Zhaoxiang Zhang. Driving into the future: Multiview visual forecasting and planning with world model for autonomous driving. *arXiv preprint arXiv:2311.17918*, 2023. 3, 4, 6

[33] Yibo Wang, Ruiyuan Gao, Kai Chen, Kaiqiang Zhou, Yingjie Cai, Lanqing Hong, Zhenguo Li, Lihui Jiang, Dit-Yan Yeung, Qiang Xu, et al. Detdiffusion: Synergizing generative and perceptive models for enhanced data generation and perception. In *CVPR*, pages 7246–7255, 2024. 1

[34] Zhou Wang, Alan C Bovik, Hamid R Sheikh, and Eero P Simoncelli. Image quality assessment: from error visibility to structural similarity. *IEEE transactions on image processing*, 13(4):600–612, 2004. 8

[35] Dongxu Wei, Zhiqi Li, and Peidong Liu. Omni-scene: Omni-gaussian representation for ego-centric sparse-view scene reconstruction. *arXiv preprint arXiv:2412.06273*, 2024. 3

[36] Yuqing Wen, Yucheng Zhao, Yingfei Liu, Fan Jia, Yanhui Wang, Chong Luo, Chi Zhang, Tiancai Wang, Xiaoyan Sun, and Xiangyu Zhang. Panacea: Panoramic and controllable video generation for autonomous driving. *arXiv preprint arXiv:2311.16813*, 2023. 3, 4, 6

[37] Guanjun Wu, Taoran Yi, Jiemin Fang, Lingxi Xie, Xiaopeng Zhang, Wei Wei, Wenyu Liu, Qi Tian, and Xinggang Wang. 4d gaussian splatting for real-time dynamic scene rendering. In *CVPR*, 2024. 5, 8, 2, 3

[38] Ziyang Xie, Junge Zhang, Wenye Li, Feihu Zhang, and Li Zhang. S-nerf: Neural radiance fields for street views. In *ICLR 2023*, 2023. 2, 3, 5, 6

[39] Yunzhi Yan, Haotong Lin, Chenxu Zhou, Weijie Wang, Haiyang Sun, Kun Zhan, Xianpeng Lang, Xiaowei Zhou, and Sida Peng. Street gaussians for modeling dynamic urban scenes. *arXiv preprint arXiv:2401.01339*, 2024. 3, 5, 1

[40] Yunzhi Yan, Zhen Xu, Haotong Lin, Haian Jin, Haoyu Guo, Yida Wang, Kun Zhan, Xianpeng Lang, Hujun Bao, Xiaowei Zhou, et al. Streetcrafter: Street view synthesis with controllable video diffusion models. *arXiv preprint arXiv:2412.13188*, 2024. 3, 1

[41] Haibo Yang, Yang Chen, Yingwei Pan, Ting Yao, Zhineng Chen, Chong-Wah Ngo, and Tao Mei. Hi3d: Pursuing high-resolution image-to-3d generation with video diffusion models. In *ACM MM*, 2024. 2

[42] Hong-Xing Yu, Haoyi Duan, Junhwa Hur, Kyle Sargent, Michael Rubinstein, William T Freeman, Forrester Cole, Deqing Sun, Noah Snavely, Jiajun Wu, et al. Wonderjourney: Going from anywhere to everywhere. In *CVPR*, 2024. 3, 4

[43] Richard Zhang, Phillip Isola, Alexei A Efros, Eli Shechtman, and Oliver Wang. The unreasonable effectiveness of deep features as a perceptual metric. In *CVPR*, 2018. 8

[44] Guosheng Zhao, Chaojun Ni, Xiaofeng Wang, Zheng Zhu, Xueyang Zhang, Yida Wang, Guan Huang, Xinze Chen, Boyuan Wang, Youyi Zhang, et al. Drivedreamer4d: World models are effective data machines for 4d driving scene representation. *arXiv preprint arXiv:2410.13571*, 2024. 3

[45] Xiaoming Zhao, R Alex Colburn, Fangchang Ma, Miguel Angel Bautista, Joshua M. Susskind, and Alex Schwing. Pseudo-generalized dynamic view synthesis from a video. In *ICLR*, 2024. 2

[46] Brady Zhou and Philipp Krähenbühl. Cross-view transformers for real-time map-view semantic segmentation. In *CVPR*, 2022. 7, 8

[47] Kaichen Zhou, Jia-Xing Zhong, Sangyun Shin, Kai Lu, Yiyuan Yang, Andrew Markham, and Niki Trigoni. Dyn-point: Dynamic neural point for view synthesis. In *NeurIPS*, 2023. 5

[48] Xiaoyu Zhou, Zhiwei Lin, Xiaojun Shan, Yongtao Wang, Deqing Sun, and Ming-Hsuan Yang. Drivinggaussian: Composite gaussian splatting for surrounding dynamic autonomous driving scenes. In *CVPR*, pages 21634–21643, 2024. 3, 5, 1

[49] Matthias Zwicker, Hanspeter Pfister, Jeroen Van Baar, and Markus Gross. Ewa volume splatting. In *Proceedings Visualization, 2001. VIS'01*, 2001. 3

Appendix (Supplementary Material)

Please find the video visualizations on our project website: <https://flymin.github.io/magicdrive3d/>

A. Further Discussion on Differences from Reconstruction Works

The main focus of this work is the generation of non-existent 3D scenes, which distinguishes it from the reconstruction of existing scenes (such as [39, 48]). While 3D scene reconstruction also leverages video generation models to enhance quality [22, 40], its goal is to produce novel views of the same scene from a given set of camera angles. In contrast, our model can directly generate entirely new 3D scenes through latent variable sampling after training. The key difference is that our approach enables the creation of entirely new scenes, a capability that reconstruction methods cannot achieve (as shown in Table 1). Specifically, our model can generate novel scenes that, while adhering to control conditions, allow for the updating of objects and environmental features, such as buildings, across different samples. Figures 1 and 6 demonstrate our method’s ability to construct diverse 3D scenes based on varying conditions. We hope this discussion helps readers gain a clearer understanding of the contribution of this work.

B. More Implementation Details

For video generation, we train our generator based on the pre-trained street view image generation model from Gao et al. [11]. By adding the proposed relative pose control, we train 4 epochs (77040 steps) on the nuScenes training set with a learning rate of $8e^{-5}$. We follow the settings for 7-frame videos described in Gao et al. [11], using 224×400 for each view but extending to $T = 16$ frames. Consequently, for 3DGS generation, we select $t = 8$ as the canonical space. Except we change the first 500 steps to optimize $(s_{c,t}, b_{c,t})$ for each view and $\lambda_{\text{reg}_o} = 1.0$, other settings are the same as 3DGS.

For the monocular depth model, we use ZoeDepth [3]. Although it is trained for metric depth estimation, due to domain differences, raw estimation is not usable, as shown in Section 5.5 and Figure 4. Methodologically, *MagicDrive3D* does not rely on a specific depth estimation model. Better estimations can further improve our scene generation quality.

Since GS only supports perspective rendering, to stitch the view for panorama, we use code provided by <https://github.com/timy90022/Perspective-and-Equirectangular> to transform from perspective to equirectangular.

All our experiments are conducted with NVIDIA V100 32GB GPUs. The generation of a single scene takes about 2 minutes for video generation and 30 minutes for GS generation. For reference, 3DGS reconstruction typically takes about 23 minutes for scenes of similar scales. Therefore, the proposed enhancement is efficient. As for rendering, there is no additional computation for our method compared with 3DGS.

As mentioned in Section 5.5, we use two testing scenarios to show the effectiveness of the enhanced GS pipeline as an ablation study, *i.e.*, 360° and vary-t. We use one testing trajectory as an example to illustrate the training/testing view splits in Table I.

name	#test	#train	camera poses
360°	6	90	
vary-t	12	84	

Table I. Two settings for ablation study on the enhanced GS pipeline. Testing views are in green while training views are in red.

C. Optimization Flow

We demonstrate the overall optimization flow of the proposed FTGS in Algorithm 1. Line 2 is the first optimization of monocular depths. Lines 4-8 refer to the second optimization of the monocular depths. Lines 10-16 are the main loop for FTGS, where we consider temporal offsets on Gaussians, camera pose optimization for local inconsistency, and AEs for appearance discrepancies among views.

D. More Ablation Study

Ablation on Offset Choice for Fault-Tolerant GS. In addition to the overall module ablation, we observe that for Fault-Tolerant GS, beyond the Gaussians’ center coordinates, their attributes (including anisotropic covariance, opacity, and har-

Table II. Ablating comparison with offsets on anisotropic covariance (Cov.), opacity, and harmonic coefficients (Features) properties in GS. We randomly sample 10 scenes from the nuScenes validation set for experiments and apply color correction (cc) to all the renderings.

Methods	L1 \downarrow	PSNR \uparrow	SSIM \uparrow	LPIPS \downarrow
3DGS	0.0733	19.7514	0.5210	0.4496
Features offset	0.0624	20.9882	0.5940	0.3463
Cov. offset	0.0632	20.8133	0.5854	0.3626
Opacity offset	0.0656	20.5332	0.5733	0.3845
Ours (xyz offset)	0.0546	21.9428	0.6288	0.2759

monic coefficients) can also be utilized to address local inconsistencies. To verify the effects of different choices, we randomly select 10 scenes from the nuScenes validation set for experimentation. As shown in Table II, the results obtained by adding offsets to the center coordinates (xyz) are the best. This aligns with our observation that local inconsistencies in the generated views occur primarily in the shape of objects, and thus, xyz displacements can most effectively resolve these inconsistencies.

Qualitative Comparison with 3DGS baseline. Figure I shows the results of reconstructing the generated video directly using the 3DGS algorithm. As discussed in Section 4.3, 3DGS tends to amplify artifacts in the generated view, whereas our improved FTGS pipeline effectively controls the impact of these artifacts, ensuring the quality of the 3D scene generation.

E. More Reconstruction Baseline

Focusing on dynamic scenes, 4DGS [37] introduces comprehensive improvements over 3DGS and achieves notable results. Therefore, we replace Fault-Tolerant GS with 4DGS. As shown in Table III, by incorporating non-rigid dynamics, 4DGS already performs better than 3DGS. However, in our task, 4DGS underperforms compared to our Fault-Tolerant GS. Based on the results in Table II, we hypothesize that our FTGS algorithm only needs to address local inconsistency caused by content inconsistency. Allocating excessive degrees-of-freedom at the representational level may hinder model convergence, thus 4DGS does not yield better results in our scenarios.

Algorithm 1 Enhanced Fault-Tolerant Gaussian Splatting (FTGS)

Require: camera views $\{\mathcal{I}_i\}$, camera parameters $\{\mathbf{P}_i^0\}$, monocular depth $\{\mathcal{D}_i\}$, optimization steps for depth s_D , camera pose s_C , and GS_{SGS}

Ensure: FTGS of the scene $\{\boldsymbol{\mu}_p, \boldsymbol{\mu}_p^o, \boldsymbol{\Sigma}_p, \text{SH}_p\}$, and optimized camera pose $\{\mathbf{P}_i^0\}$

- 1: $\mathcal{P}_{SfM} = \text{PCD from SfM}$
- 2: Optimize $(s_{c,t}, b_{c,t})$ with \mathcal{P}_{SfM} for each $\{c, t\}$
- 3: Random initialize AEs $\{\mathbf{e}_i\}$
- 4: **for** step in $1, \dots, s_D$ **do**
- 5: Random pick one view \mathcal{I}_i
- 6: $\mathcal{L} = \mathcal{L}_{\text{AEGS}}(\mathcal{I}_i, \mathcal{I}_i^r, \mathbf{e}_i)$
- 7: Update $(s, b), \mathbf{e}_i, \boldsymbol{\Sigma}, \text{SH}$ with $\nabla \mathcal{L}$
- 8: **end for**
- 9: Initialize $\boldsymbol{\mu}$ with (s, b) and \mathcal{D}
- 10: **for** step in s_D, \dots, s_{GS} **do**
- 11: Random pick one view \mathcal{I}_i and get its t
- 12: $\mathcal{L} = \mathcal{L}_{\text{FTGS}}(\mathcal{I}_i, \mathcal{I}_i^r, \mathbf{e}_i, \boldsymbol{\mu}^o(t))$
- 13: Update $\boldsymbol{\mu}, \boldsymbol{\mu}^o(t), \mathbf{e}_i, \boldsymbol{\Sigma}, \text{SH}$ with $\nabla \mathcal{L}$
- 14: **if** step $> s_C$ **then**
- 15: Update \mathbf{P}_i^0 with $\nabla \mathcal{L}$
- 16: **end if**
- 17: **end for**

Original 3DGS (w/ nuScenes dataset)



Ours (w/ nuScenes dataset)



Figure I. Qualitative Comparison with 3DGS baseline on the same scene shown in Figure 5. With our improved FTGS pipeline, the generated 3DGS contains fewer floaters, leading to higher-quality rendering.

Table III. Comparison with 4DGS [37]. We randomly sample 10 scenes from the nuScenes validation set for experiments and apply color correction (cc) to all the renderings.

Methods	L1 ↓	PSNR ↑	SSIM ↑	LPIPS ↓
3DGS	0.0733	19.7514	0.5210	0.4496
4DGS	0.0601	21.1195	0.5892	0.4475
Ours	0.0546	21.9428	0.6288	0.2759

F. Limitation and Future Work

As a data-centric method, *MagicDrive3D* sometimes struggles to generate complex objects like pedestrians, whose appearances are intricate. Additionally, areas with much texture detail (e.g., road fences) or small spatial features (e.g., light poles) are occasionally poorly generated due to limitations in the 3DGS method. Future work may focus on addressing these challenges and further improving the quality and robustness of generated 3D scenes.

G. Comparison with Simple Baselines

As shown in Figure II, we further compare *MagicDrive3D* with two baselines, *i.e.*, *LucidDreamer* [7] and *WonderJourney* [42]. The former method has been proposed recently and takes text description as the only condition. Thus, it is hard to generate photo-realistic street scenes. When providing multi-view video frames from nuScenes with known camera poses, their pipeline fails to reconstruct. We suppose the reason is limited overlaps and errors from depth estimation. As suggested by the released code, we changed the image generation model to `lillyasviel/control-v11p_sd15_inpaint` for inpainting by providing a nuScenes image, *i.e.*, Figure IIa. However, due to the lack of controllability, the results from *LucidDream* (*e.g.*, Figure IIb) are unsatisfactory. On the other hand, due to the lack of control over objects within the scene, *WonderJourney* struggles to generate coherent scenes. Inpainting-based methods like the two above exhibit a pronounced sense of patches and face significant challenges in achieving 360° coverage.

Figure II^d further shows directly stitching real data. It is also bad due to the limited overlaps between views. On the contrary, the scene generated from *MagicDrive3D* can render a continuous panorama, as shown in Figure II^e, which is also controllable through multiple conditions.

Note that, panorama generation is only one of the applications of our generated scenes. We show them just for convenient qualitative comparison within the paper. Since our scene generation contains geometric information, it can be rendered from any camera view, as shown in Figure 5.

H. Implementation Detail of Appearance Embedding

We show in Figure III the detailed architecture of the CNN used in our appearance modeling. The AE map is 32× smaller than the input image to reduce the computational cost. Hence, we first downsample the input image by 32×. Then, we use 3×3 convolution for feature extraction and pixel shuffle for upsampling. Each convolution layer is activated by ReLU.



(a) Conditional image to LucidDreamer [7]



(b) Scene generated by LucidDreamer [7], with text “A driving scene in the city from the front camera of the vehicle. A bus on the right side. There is a bridge overhead. There is a railing in the center of the left road. Some vehicles ahead”



(c) Scene generated by WonderJourney [42]. We set the focal length to be the same as the conditional image. WonderJourney cannot control road semantics (many objects are physically implausible) and fails in loop closure for 360° scene generation. Conditions are the same as Figure IIb.



(d) Stitched panorama with real camera views from nuScenes dataset. Due to the limited overlaps, there are many empty (black) areas.



(e) Panorama from *MagicDrive3D*. The scene is generated with the same object boxes and BEV map as Figure IIc, but turned to “rainy day”.

Figure II. Comparison with two baselines (LucidDreamer [7] and WonderJourney [42]) and direct stitching real images.

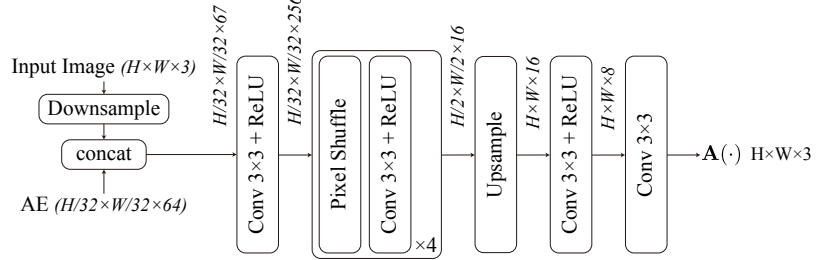


Figure III. The CNN architecture of appearance modeling, as introduced in Section 4.3.

I. Broader Impacts

The implementation of *MagicDrive3D* in controllable 3D street scene generation could potentially revolutionize the autonomous driving industry. By creating detailed 3D scenarios, self-driving vehicles can be trained more effectively and efficiently for real-world applications, thereby leading to improved safety and accuracy. Moreover, it could potentially provide realistic simulations for human-operated vehicle testing and training, thus contributing to reducing the occurrence of accidents on the roads while enhancing driver expertise. In the broader scope, *MagicDrive3D* could be of considerable value to the virtual reality industry and video gaming industry, enabling these sectors to generate more lifelike 3D scenes and intricate gaming experiences.

On the downside, the development and application of such advanced technology could lead to certain unwanted scenarios. For instance, the increased automation in industries, driven by the potential of this technology, could lead to job losses for

drivers and other related professionals as their roles become automated. A societal transition will be needed to avoid negative impacts on employment levels and the fairness of wealth distribution.

J. More Qualitative Results

We show more generated street scenes from *MagicDrive3D* in Figure IV and Figure V.



Figure IV. Generated street scenes from *MagicDrive3D*. We adopt control signals from the nuScenes validation set. We crop the center part for better visualization.

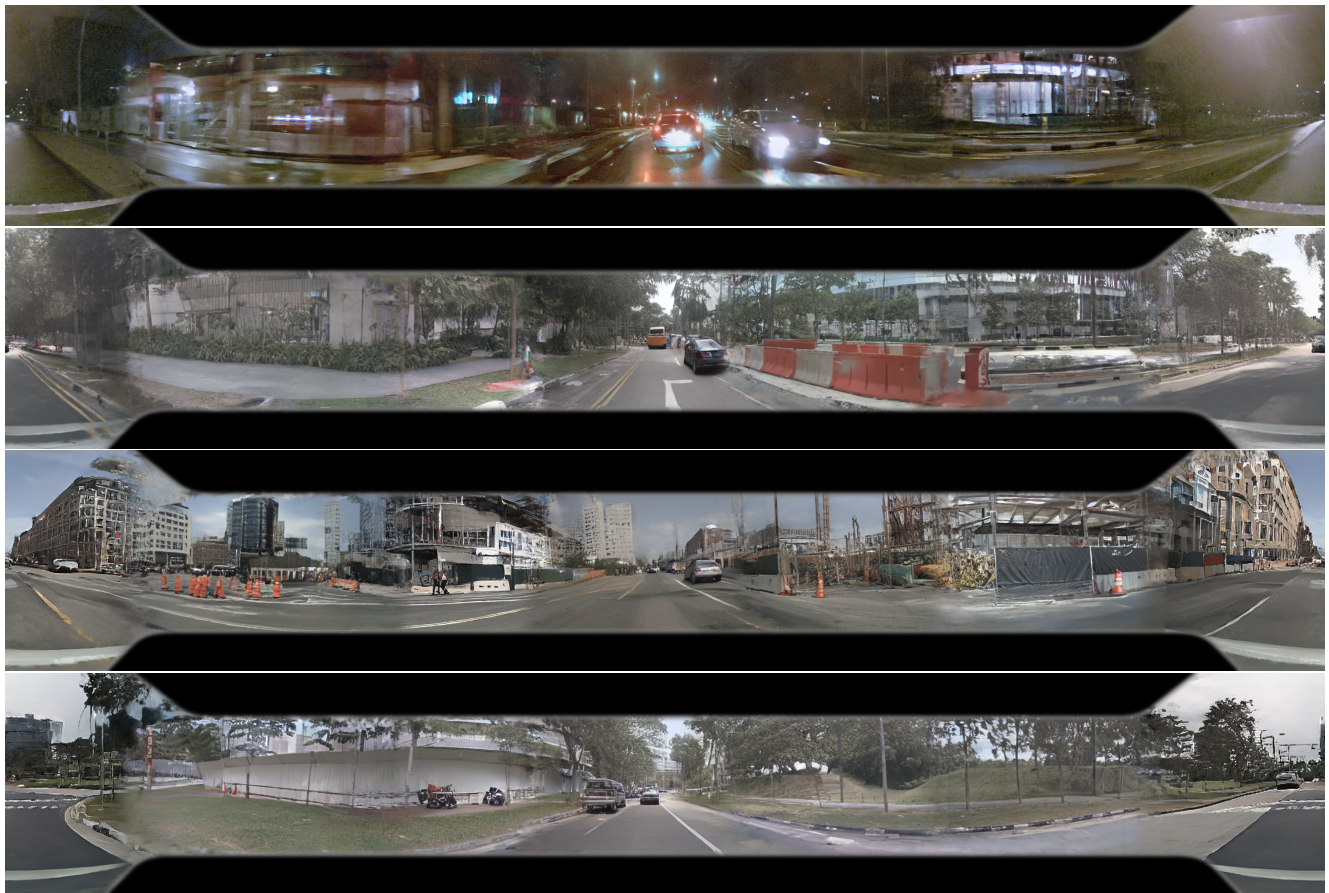


Figure V. Generated street scenes from *MagicDrive3D*. We adopt control signals from nuScenes validation set. The black regions are not fully covered, constrained by the camera's FOV.